

Research Paper

The ZFOURGE luminosity function - I. Extending the faint end of MIPS selected galaxies to $z \simeq 6$

Daniel J. Lyon¹, Michael J. Cowley¹ and Andrew M. Hopkins²

¹School of Chemistry and Physics, Queensland University of Technology, Brisbane, QLD, Australia and ²Australian Astronomical Optics, Macquarie University, North Ryde, NSW, Australia

Abstract

Lorem ipsum dolor sit amet, consectetur adipiscing elit. Ut purus elit, vestibulum ut, placerat ac, adipiscing vitae, felis. Curabitur dictum gravida mauris. Nam arcu libero, nonummy eget, consectetur id, vulputate a, magna. Donec vehicula augue eu neque. Pellentesque habitant morbi tristique senectus et netus et malesuada fames ac turpis egestas. Mauris ut leo. Cras viverra metus rhoncus sem. Nulla et lectus vestibulum urna fringilla ultrices. Phasellus eu tellus sit amet tortor gravida placerat. Integer sapien est, iaculis in, pretium quis, viverra ac, nunc. Praesent eget sem vel leo ultrices bibendum. Aenean faucibus. Morbi dolor nulla, malesuada eu, pulvinar at, mollis ac, nulla. Curabitur auctor semper nulla. Donec varius orci eget risus. Duis nibh mi, congue eu, accumsan eleifend, sagittis quis, diam. Duis eget orci sit amet orci dignissim rutrum.

Keywords: galaxies: luminosity function, mass function; cosmology: observations; infrared: galaxies; galaxies: evolution

(Received xx xx xxxx; revised xx xx xxxx; accepted xx xx xxxx)

1. Introduction

Galaxy luminosity functions (LF) are statistical distributions that describe the spatial density of galaxies at different luminosities and are a fundamental tool for quantifying their evolution across cosmic time scales (Han et al. 2012; Dai et al. 2009; Wylezalek et al. 2014).

By splitting the data into redshift bins, an accurate picture of galaxy distribution and evolution is acquired. The differences in the bins provide insight into how galaxies have evolved through time and point to periods of increased or decreased activity. ZFOURGE allows us to look at the infrared (IR) LF of galaxies with increased depth, extending the LF to potentially redshift of $z \approx 6$.

In section 2 we ... In section 3 we ... In section 4 we ... In section 5 we ... In section 6 we ...

This paper is the first in a 2-part series, with the second looking at the ZFOURGE AGN LF and our approach to using CIGALE to decompose the IR SED and purely recover the AGN component.

We adopt a cosmology of $H_0 = 70 \text{ km s}^{-1} \text{ Mpc}^{-1}$, $\Omega_m = 0.7$, and $\Omega_\Lambda = 0.3$.

Research by Wu et al. (2011) has shown that the UV and optical wavelengths closely follow a Schechter function. In contrast, the IR wavelengths have a shallower exponential which is inconsistent with a Schechter function. Fu et al. (2010) proposed that this difference is due to the AGN contribution to the IR Galaxy LF. Even though this research primarily focuses on IR AGN LFs, it is essential to compare the IR Galaxy LF differences which this paper focuses on. In the next paper, we dive into IR AGN LFs.

Galaxy luminosity distribution and the environment have often been used to provide strong constraints of theories of galaxy evolution Biviano et al. (2011)

powerful constraints on how galaxies evolve in relation to their environment are expected to be obtained from the analysis of the galaxy IR LFs. Biviano et al. (2011)

IR data can give information only for dusty massive galaxies and are limited especially at high redshifts Katsianis et al. (2017)

alpha, the faint end slope of the galaxy LF, does not evolve significantly with redshift. Wylezalek et al. (2014)

Confirm that evolution on both luminosity and density is required to explain the difference in the LFs at different redshifts. Wu et al. (2011)

Extensively studied at low redshift. Wu et al. (2011)

SF may also heat the dust in galaxies and lead to excess emission in the longer wavelengths O'Connor et al. (2016)

The SF fraction is also found to be a function of luminosity/redshift, decreasing as luminosity/redshift increases, while the trend is more obvious in the MIR, suggesting that the MIR wavelength is more sensitive to the presence of AGNs Wu et al. (2011)

Star forming galaxies reemit a significant portion of the ultraviolet and optical radiation absorbed by dust in the infrared regime. Symeonidis and Page (2021); Fu et al. (2010)

The obscured or absorbed optical, UV and X-ray radiation will be re-emitted in the IR. Han et al. (2012); Brown et al. (2019)

The IR-bright, dust obscured galaxy population is crucial to understanding galaxy formation and evolution. Gruppioni et al. (2011)

IR bright galaxies emit the bulk of their energy as dust-reprocessed light generated by dusty SF or accretion onto the supermassive black holes referred to hereafter as active galactic nuclei. Wu et al. (2011)

Author for correspondence: Daniel Lyon, Email: daniellyon31@gmail.com

Cite this article: Author1 C and Author2 C, an open-source python tool for simulations of source recovery and completeness in galaxy surveys. *Publications of the Astronomical Society of Australia* 00, 1–12. <https://doi.org/10.1017/pasa.xxxx.xx>

Absorption by dust reprocesses the shorter wavelength radiation from the accretion disk into mid/far-IR continuum radiation. Assef *et al.* (2011)

The evolution of star formation activity in galaxies over cosmic history, and the physical process which may drive and limit such activity, have been the subject of intense observational and theoretical study in recent years. Grazian *et al.* (2015)

2. The ZFOURGE Survey

2.1. Overview

The data for analysis is readily accessible through the ZFOURGE database at VizieR^a (Straatman *et al.* 2016). This dataset encompasses all three 11×11 arcminute fields within the ZFOURGE survey: the Chandra Deep Field South (CDFS), located at coordinates RA: 10h 00m 31s and DEC: +02° 17' 03" (Giacconi *et al.* 2002); the Cosmic Evolution Survey (COSMOS), located at RA: 03h 32m 27s and DEC: −27° 45' 52" (Scoville *et al.* 2007); and the CANDELS Ultra Deep Survey (UDS), located at RA: 02h 17m 15s and DEC: −05° 11' 53" (Lawrence *et al.* 2007). To ensure a comprehensive selection of candidate galaxies and minimise errors, the sole criterion applied is the Use=1 category, ensuring the inclusion of well-defined galaxies based on redshift, distance, magnitude, and other characteristics. The ZFOURGE dataset extends up to redshift $z \simeq 6$, providing a broad view across different epochs, particularly within the critical cosmic periods around $1 < z < 3$ (Gruppioni *et al.* 2011; Wylezalek *et al.* 2014), where luminous density peaks before diminishing (Assef *et al.* 2011).

Our analysis is based on galaxies from the 2017 release of the ZFOURGE survey (Straatman *et al.* 2016). This survey comprises approximately 70,000 galaxies at redshifts greater than 0.1, observed using the near-infrared FourStar imager (Persson *et al.* 2013) mounted on the 6.5-m Magellan Baade Telescope at the Las Campanas Observatory in Chile. ZFOURGE employs deep near-infrared imaging in multiple medium-band filters (J1, J2, J3, H1, Hs) and a broad-band Ks filter. The imaging spans 1.0 to 1.8 μm and achieves 5 σ point-source limiting depths of 26 AB mag in the J medium-bands and 25 AB mag in the H and Ks bands (Spitler *et al.* 2012). These filters yield well-constrained photometric redshifts, particularly effective for sources within the redshift range of 1 to 4 (Spitler *et al.* 2012). ZFOURGE data is supplemented by public data from HST/WFC3 F160W and F125W imaging from the CANDELS survey, as well as data from Spitzer/Infrared Array Camera (IRAC) and Herschel/Photodetector Array Camera and Spectrometer (PACS). For a detailed description of the data and methodology, refer to Straatman *et al.* (2016).

2.2. Sample Selection

The three combined field, CDFS, COSMOS, and UDS have a combined total of 73,790 unique galaxies, but we employ some data reduction techniques to improve the quality of final dataset. First, we limit our sample to galaxies well defined by many factors such as sign-to-noise ratio, removing stars, bad detections, good redshifts, and more. This is given by keeping all sources with the column Use=1 in the dataset and immediately reduces the sample to 37,647 galaxies. Additionally, we keep all sources with a bolometric IR (8-1000 μm) luminosity $L_{\text{bol}} \geq 0$. This is a simple data mask that only keeps galaxies whose bolometric IR luminosity has

been successfully calculated and has further reduced our dataset to 22,997 galaxies. Finally, we utilise the ZFOURGE AGN catalogues provided by Cowley *et al.* (2016) to remove AGN from our sample. The AGN catalogues are similar to the Use data column with three new columns of irAGN, radAGN, and xAGN where a 1 in any column denotes a positive AGN. These three columns are ORed together and 552 galaxies across the three fields are removed, leaving a sample of 22,472 galaxies.

ZFOURGE can stretch up to redshift $z \simeq 6$, (with the highest redshift in the sample detected all the way out to $z = 7.9691$; only 28 galaxies greater than $z = 6$ exist in ZFOURGE) allowing us to study a wide range of epochs. Our final sample includes 22,444 galaxies. This data range enables us to observe the evolution of galaxies during some of the most critical cosmic periods, specifically around $1 < z < 3$ (Gruppioni *et al.* 2011; Wylezalek *et al.* 2014). In the following section we detail the process of calculating the bolometric IR luminosity.

move UVJ here. Also Quiescent and star-forming

3. Bolometric IR Luminosity Derivation

The bolometric IR luminosity is defined and calculated by integrating under the best-fit SED of each source from 8-1000 μm . Specifically, the averaged Wuyts *et al.* (2008) template is used to fit the 24-160 μm photometry and the total 8-1000 μm bolometric IR luminosity is then estimated from the best fit. Refer to section 6 of Straatman *et al.* (2016) for a full description of the bolometric IR luminosity calculation. We use the bolometric IR luminosities to calculate the bolometric IR luminosity function of the ZFOURGE survey up to $z \approx 6$ (see sections 4 and 5.1).

As a result of the SED fitting process, the flux limit of the ZFOURGE survey varies with redshift. (see figure 1, left). We use the ZFOURGE 24 μm flux limit (3 μJy) as a proxy for the bolometric flux limit (Rodighiero *et al.* 2010). Typically, the flux limit is constant with redshift and will produce a hard edge detection limit (Malmquist 1922) that is defined by the luminosity-distance relationship (equation 1).

$$L = 4\pi D_L^2 F \quad (1)$$

Where L is the luminosity, D_L is the luminosity-distance, and F is the galaxy flux. We correct for the varying flux limit by defining a single flux limit for each redshift bin of the luminosity function. Each new flux limit is derived by taking a percentile cut of the bolometric flux (equation 2) from each redshift bin such that there is no incompleteness. The flux limit of each redshift bin is shown in figure 1 (right) coloured by redshift bin and listed in table 1. Additionally, luminosity completeness limits are calculated for each redshift bin and are defined by the minimum luminosity that a galaxy must have for its maximum distance to be located at the end of the redshift bin. These completeness limits are listed in table 1 and displayed in figure 2 as vertically dashed violet lines.

$$F_{\text{bol}} = \frac{L_{\text{bol}}}{4\pi D_L^2} \quad (2)$$

4. Luminosity Functions

4.1. Vmax

To estimate the luminosity function from our data, we utilise the $1/V_{\text{max}}$ method (Schmidt 1968). The $1/V_{\text{max}}$ method does not make any assumptions or depend on the shape of the luminosity

^aZFOURGE Data: <http://vizier.cds.unistra.fr/viz-bin/VizieR?-source=J/ApJ/830/51&-to=2>

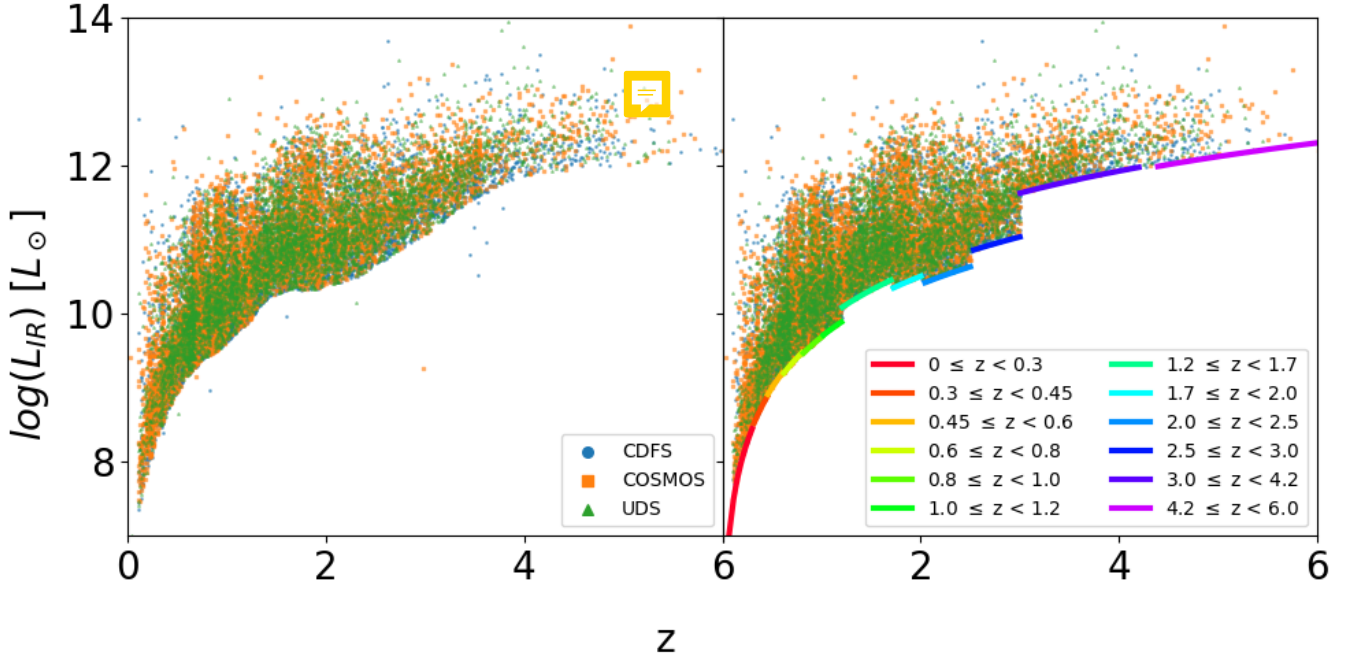


Figure 1. Left: Bolometric IR Luminosity as a function of redshift across the 3 ZFOURGE Fields with the $24\mu\text{m}$ flux limit of 0.003mJy . CDFS is represented by blue-filled circles, COSMOS by orange-filled squares, and UDS by green-filled triangles. Right: Sources with fluxes below the bolometric flux limit of each redshift bin according to table 1 are removed. These flux limits are shown as the coloured lines. The luminosity completeness limits are a hard and straight cut in each redshift bin defined as the minimum luminosity a galaxy requires for its maximum possible distance to reach the end of the redshift bin. This corrects for the incomplete shape of the luminosity-distance relation by having a separate maximum distance for each redshift bin.

Table 1. Bolometric flux and luminosity limits for each redshift bin.

z	$F_{\text{lim}}^{\text{bol}} \times 10^{-18} \text{ (W/m}^2\text{)}$	$\log_{10}(L_{IR}/L_{\odot})$
$0.00 \leq z < 0.30$	3.73	8.45
$0.30 \leq z < 0.45$	3.87	8.88
$0.45 \leq z < 0.60$	4.01	9.19
$0.60 \leq z < 0.80$	3.76	9.47
$0.80 \leq z < 1.00$	3.56	9.69
$1.00 \leq z < 1.20$	3.61	9.89
$1.20 \leq z < 1.70$	5.62	10.45
$1.70 \leq z < 2.00$	4.26	10.51
$2.00 \leq z < 2.50$	3.32	10.64
$2.50 \leq z < 3.00$	5.41	11.04
$3.00 \leq z < 4.20$	21.1	11.98
$4.20 \leq z < 6.00$	19.5	12.31

function itself, making this method a very reliable model of the LF shape. The $1/V_{\text{max}}$ accounts for the maximum observable volume of each galaxy and is given by equation 3.

$$\phi(L, z) = \frac{1}{\Delta \log L} \sum_{i=1}^N \frac{1}{V_{\text{max},i}} \quad (3)$$

where V_{max} represents the maximum co-moving volume of the i -th source and $\Delta \log(L)$ is the width of the luminosity bin. In practice, to observe the evolution of the luminosity function through cosmic time, the maximum observable volume (V_{max}) is calculated for each redshift bin where the volume is limited by the upper and lower bounds of the redshift bin. For example, galaxies above 10^{12}

L_{\odot} appearing in the first redshift bin $0.00 \leq z < 0.30$ have a maximum distance and volume corresponding to $z = 0.30$, even though such galaxies could potentially be detected up to $z = 4$ with the same flux limit. Additionally, redshift bins are split by luminosity bins to observe the number density evolution across the different classes of luminosity such as LIRGS ($10^{11} < L_{IR} < 10^{12} L_{\odot}$) and ULIRGS ($L_{IR} > 10^{12} L_{\odot}$). V_{max} of each galaxy is calculated by taking the maximum comoving-volume of the redshift bin the galaxy resides in and subtracting the comoving-volume at the beginning of the redshift bin (equation 3). We account for the survey area probed by ZFOURGE (0.1111 degrees^2) which normalises the volume probed across the whole sky ($41,253 \text{ degrees}^2$).

$$V_{\text{max},i} = \frac{4}{3} \pi (D_{\text{max}}^3 - D_{\text{min}}^3) \times \frac{\text{area}}{41,253} \quad (4)$$

As a consequence of the luminosity completeness limits defined at the end of section 3 (and in table 1), the volume probed for a galaxy in a redshift bin is the same for all galaxies in the same redshift bin. Different redshift bins have different volumes and each luminosity bin has a different number density ϕ . Therefore, D_{min} and D_{max} are the comoving-distances at the beginning and end of the redshift bin respectively. We calculate D_{max} and D_{min} using `astropy.cosmology.FlatLambdaCDM.comoving_distance` (Astropy Collaboration et al. 2022) for all sources in each redshift bin above the luminosity-completeness limits defined in table 1. We limit each luminosity bin to a minimum of 5 sources, or else the luminosity bin is discarded. The relative LF number density error values are calculated with:

$$\phi(L, z) = \frac{1}{\Delta \log L} \sqrt{\sum_i \frac{1}{V_{\text{max}}^2}} \quad (5)$$

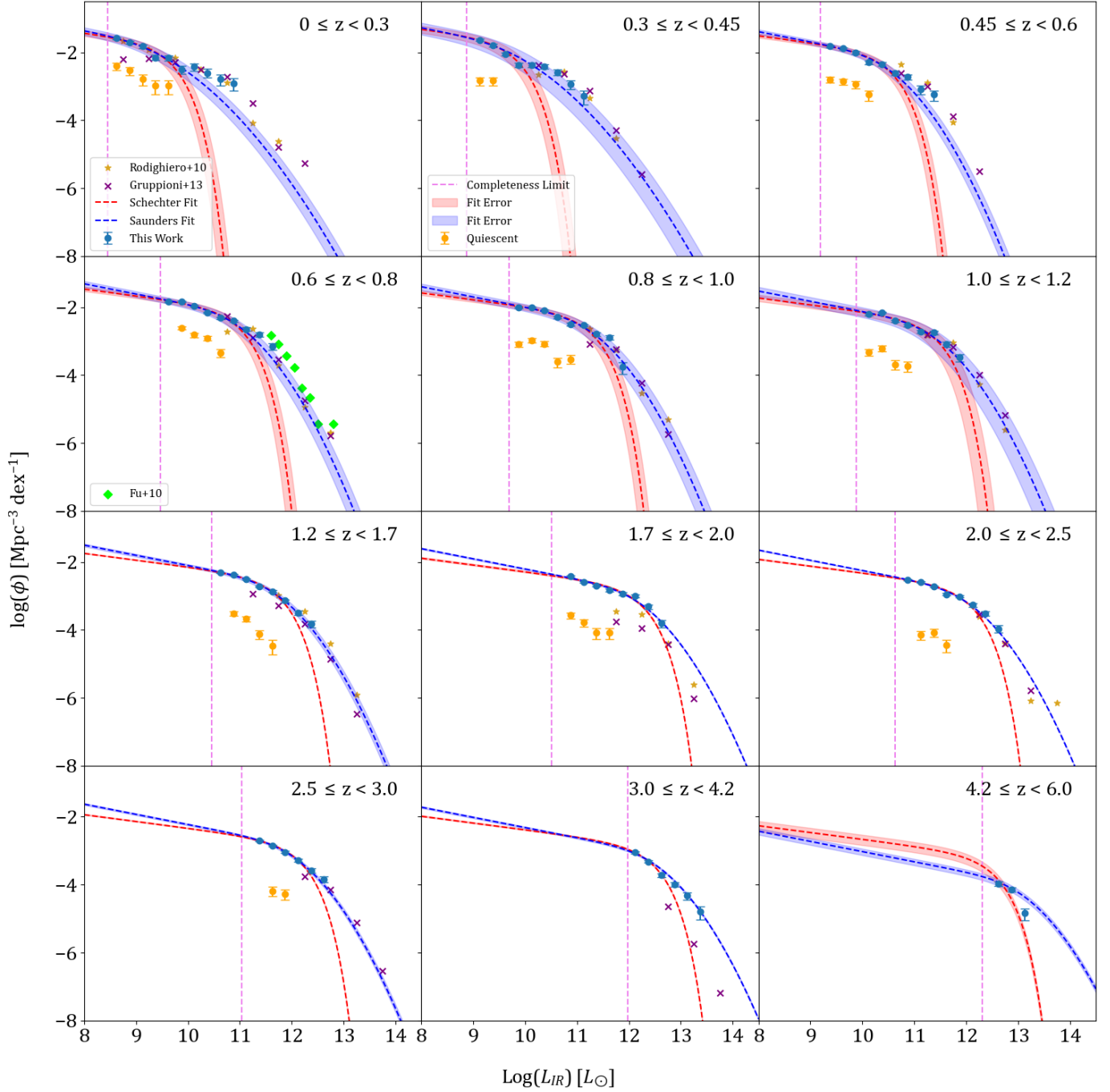


Figure 2. The ZFOURGE Bolometric IR (8-1000 μ m) LF. Blue circle points represent the LF of the three combined ZFOURGE fields of CDFS, COSMOS, and UDS, calculated using the Vmax method. The blue dashed line shows the best fit Saunders function (Saunders et al. 1990) with one standard deviation fit errors to our data. Similarly, the best fit Schechter function (Schechter 1976) and one standard deviation fit error is shown in red as a comparison. The ZFOURGE quiescent LF is shown as orange filled circles. The luminosity completeness limit of each redshift bin is shown as the violet dashed line. Where possible, comparable literature results are also shown. Rodighiero et al. (2010) is shown as gold filled stars. Gruppioni et al. (2013) is shown as purple crosses. Fu et al. (2010) is shown as green diamonds.

4.2. Fitting Functions

To model LFs, one of the most widely used methods is the Schechter function (Schechter 1976) (equation 6). This function is beneficial for describing the LF of galaxies because it can represent observed features such as a power-law decline at the faint end and an exponential cutoff at the bright end.

$$\phi(L) = \phi^* \left(\frac{L}{L^*} \right)^{1-\alpha} \exp \left(-\frac{L}{L^*} \right) \quad (6)$$

Where $\phi(L)$ is the number of galaxies per unit volume (number density), ϕ^* is the characteristic normalisation factor, L is the bolometric IR (8-1000 μ m) luminosity, L^* is the characteristic luminosity, and α is the faint end slope (Schechter 1976). However, the Schechter function is not the best-fitting function at

Table 2. Low redshift bolometric IR (8-1000 μ m) LF ϕ values calculated using the 1/Vmax method.

$\log_{10}(L_{IR}/L_{\odot})$	$0.00 \leq z < 0.30$	$0.30 \leq z < 0.45$	$0.45 \leq z < 0.60$	$0.60 \leq z < 0.80$	$0.80 \leq z < 1.00$	$1.00 \leq z < 1.20$
8.625	-1.58 ± 0.04	-	-	-	-	-
8.875	-1.70 ± 0.05	-	-	-	-	-
9.125	-1.82 ± 0.05	-1.64 ± 0.03	-	-	-	-
9.375	-2.15 ± 0.08	-1.79 ± 0.04	-1.82 ± 0.03	-	-	-
9.625	-2.16 ± 0.08	-2.05 ± 0.05	-1.89 ± 0.03	-1.83 ± 0.02	-	-
9.875	-2.51 ± 0.13	-2.37 ± 0.07	-2.01 ± 0.04	-1.83 ± 0.02	-2.00 ± 0.02	-
10.125	-2.43 ± 0.12	-2.37 ± 0.07	-2.29 ± 0.05	-1.97 ± 0.02	-2.00 ± 0.02	-2.21 ± 0.03
10.375	-2.60 ± 0.15	-2.41 ± 0.08	-2.34 ± 0.05	-2.16 ± 0.03	-2.09 ± 0.02	-2.16 ± 0.02
10.625	-2.78 ± 0.19	-2.58 ± 0.10	-2.61 ± 0.08	-2.32 ± 0.04	-2.30 ± 0.03	-2.41 ± 0.03
10.875	-2.90 ± 0.23	-2.94 ± 0.16	-2.72 ± 0.09	-2.41 ± 0.04	-2.50 ± 0.04	-2.53 ± 0.04
11.125	-	-3.28 ± 0.26	-3.09 ± 0.14	-2.65 ± 0.06	-2.53 ± 0.04	-2.71 ± 0.05
11.375	-	-	-3.25 ± 0.18	-2.80 ± 0.07	-2.79 ± 0.06	-2.75 ± 0.05
11.625	-	-	-	-3.15 ± 0.10	-2.89 ± 0.06	-3.10 ± 0.08
11.875	-	-	-	-	-3.76 ± 0.21	-3.48 ± 0.12

Note: Luminosity bin values are centred. Bins are 0.25 $\log_{10}(L_{\odot})$ wide: $= \pm 0.125$ either side.

Table 3. High redshift bolometric IR (8-1000 μ m) LF ϕ values calculated using the 1/Vmax method.

$\log_{10}(L_{IR}/L_{\odot})$	$1.20 \leq z < 1.70$	$1.70 \leq z < 2.00$	$2.00 \leq z < 2.50$	$2.50 \leq z < 3.00$	$3.00 \leq z < 4.20$	$4.20 \leq z < 6.00$
10.625	-2.32 ± 0.03	-	-	-	-	-
10.875	-2.37 ± 0.02	-2.43 ± 0.02	-	-	-	-
11.125	-2.51 ± 0.02	-2.59 ± 0.03	-2.53 ± 0.02	-	-	-
11.375	-2.72 ± 0.03	-2.70 ± 0.03	-2.58 ± 0.02	-2.69 ± 0.02	-	-
11.625	-2.87 ± 0.03	-2.83 ± 0.04	-2.72 ± 0.03	-2.85 ± 0.03	-	-
11.875	-3.14 ± 0.04	-2.94 ± 0.04	-2.95 ± 0.03	-3.04 ± 0.04	-	-
12.125	-3.49 ± 0.07	-2.99 ± 0.05	-3.02 ± 0.04	-3.29 ± 0.05	-3.05 ± 0.02	-
12.375	-3.82 ± 0.10	-3.31 ± 0.07	-3.27 ± 0.05	-3.58 ± 0.07	-3.32 ± 0.03	-
12.625	-	-3.81 ± 0.13	-3.52 ± 0.07	-3.84 ± 0.10	-3.72 ± 0.05	-3.97 ± 0.06
12.875	-	-	-3.97 ± 0.12	-	-3.98 ± 0.08	-4.14 ± 0.08
13.125	-	-	-	-	-4.32 ± 0.12	-4.84 ± 0.21
13.375	-	-	-	-	-4.80 ± 0.23	-

Note: Luminosity bin values are centred. Bins are 0.25 $\log_{10}(L_{\odot})$ wide: $= \pm 0.125$ either side.

mid- and far-IR wavelengths (Cite). The bright end slope of the Schechter function is too steep to fit our data (see figure 2), in agreement with the literature (Rodighiero et al. 2010; Gruppioni et al. 2013). To better fit our data, we make use of a modified Schechter function known as the Saunders function (Saunders et al. 1990) (equation 7). Where the parameters are the same as the Schechter function (equation 6), but with the introduction of σ to vary the bright end slope.

$$\phi(L) = \phi^* \left(\frac{L}{L^*} \right)^{1-\alpha} \exp \left[-\frac{1}{2\sigma^2} \log_{10}^2 \left(1 + \frac{L}{L^*} \right) \right] \quad (7)$$

Our deep ZFOURGE data probes to very faint luminosities across redshift, thus better constraining the faint end of the LF. At our lowest redshift bins, we do not have comparatively high luminosity bins to fit the bright end of the luminosity function. We perform the fitting process only on our data and do not use literature data points to constrain the luminosity function, instead opting

to fix α and σ with values matching the bright end of the literature across each redshift bin. This gives us a pure evolution in L^* and ϕ^* which is shown in figure 4 and listed in tables 4 split bolo LF param evolution table into Schechter and Saunders.

5. Discussion

5.1. Bolometric IR LF

We fit the Schechter function (Schechter 1976) (equation 6) in red and the Saunders' function (Saunders et al. 1990) (equation 7) in blue in figure 2. We use `scipy.optimize.curve_fit` (Virtanen et al. 2020) to perform the fitting and calculate 1σ relative parameter dispersion errors (shown as the transparent red and blue-filled lines respectively) using the equation: `perr = np.sqrt(np.diag(pcov))`. `perr` relates the covariance of each individual fit; all redshift bins show a fit error, but in some, the covariance is very small.

With the ZFOURGE bolometric IR (8-1000 μ m) LF across all redshift bins now calculated (figure 2), the results can be compared to the literature. We compare our results with Rodighiero *et al.* (2010) across redshift bins from $0 \leq z < 2.5$ as gold stars; Gruppioni *et al.* (2013) as purple crosses from $0 \leq z < 4.2$; and Fu *et al.* (2010) as green diamonds from $0.6 \leq z < 0.8$. There is very good agreement with the results from the literature in all bins except $1.7 \leq z < 2$ and $3.0 \leq z < 4.2$, which we will discuss shortly. Across all redshift bins, we consistently see that the ZFOURGE ϕ values in blue extend much fainter than the rest of the literature, showcasing ZFOURGE’s ability to probe to fainter luminosities. This allows us to better constrain the faint end slope of the luminosity function, which we do by fixing $\alpha = 1.3$ across all bins for the Saunders’ function fit (Saunders *et al.* 1990) (equation 7). In the Schechter function fit (Schechter 1976) (equation 6), we fix $\alpha = 1.2$, and a noticeable difference between the two functions at the faint end is seen with the Saunders function increasing higher. This result differs from the literature where Rodighiero *et al.* (2010); Gruppioni *et al.* (2013) fix $\alpha = 1.2$ whereas Fu *et al.* (2010) leaves α as a free fitting parameter found to be $\alpha = 1.46$ (respective to our Saunders function). The faint end of the bolometric LF is better constrained in ZFOURGE, of which we find an α value of 1.3 is a better fit. Although ZFOURGE can probe fainter luminosities, there is still room to improve constraints at the faint of the LF. At lower redshifts ($0.00 \leq z < 1.20$), lowering the completeness limit of each redshift bin by a single order of luminosity in $\log(L_{IR}/L_{\odot})$ space would be sufficient to well-constrain the faint end of the LF. At higher redshifts ($z \geq 1.20$), the completeness limit would need to be lowered by 1-2 orders of luminosity to constrain the faint end slope.

The bright end slope of a Schechter function is too steep to accurately describe the IR LF (Wu *et al.* 2011). Although, Fu *et al.* (2010) reports that the star-forming mid-IR LFs are accurately modelled by a Schechter function, meaning there is potentially AGN contamination in our data. Wu *et al.* (2011) also agrees that the removal of AGN sources will show a better Schechter fit. We use AGN selection catalogues provided by Cowley *et al.* (2016) to remove AGN identified sources from the galaxy, star-forming, and quiescent luminosity functions. Even after removing AGN identified galaxies (552), our results do not show any noticeably improved Schechter function fit as predicted by Fu *et al.* (2010); Wu *et al.* (2011).

The completeness limit for each redshift bin was defined in section 3, are listed in table 1, and shown as violet dashed lines in figure 2. Galaxies whose maximum comoving-distance is located at the end of the redshift bin, but have luminosities below the luminosity-distance limit are removed. The only galaxies in each redshift bin are galaxies whose maximum distance is the end of the redshift bin and thus galaxies whose maximum distance is less than the end of the redshift bin are removed.

The ZFOURGE quiescent LF is shown in figure 2, however, the SF LF was calculated but is not displayed because it is almost identical to the total IR LF. We use the UVJ colour-colour diagram to differentiate between quiescent and star-forming galaxies by selecting a quiescent galaxy mask with equation 8 (Cowley *et al.* 2016). *better reference?* U, V, & J are the rest-frame Johnson U, V and 2MASS J filters respectively. (Straatman *et al.* 2016). Star-forming galaxies are selected by taking the inverse of the quiescent galaxy mask. Quiescent luminosity bins exist from $0.000 \leq z < 3.00$, after which the remaining quiescent galaxies fall below our minimum number count of 5 galaxies. The quiescent and star-forming galaxies follow the same completeness limits and

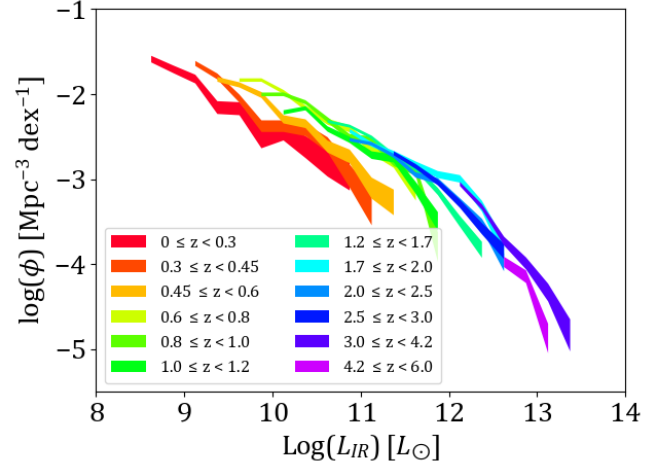


Figure 3. Combined evolution of the ZFOURGE bolometric IR (8-1000 μ m) LF. Data points are colour filled between the lower and upper uncertainties.

have maximum luminosity distances at the end of the redshift bin. We do not recalculate the bolometric flux limits for each redshift bin and instead continue using the total IR LF limits defined in table 1.

$$\begin{aligned} U - V &> 1.3, \\ V - J &< 1.6, \\ U - V &> 0.88 \times (V - J) + 0.59 \end{aligned} \quad (8)$$

On the redshift bins $1.7 \leq z < 2$ and $3.0 \leq z < 4.2$, ZFOURGE results show much higher ϕ values across all luminosity bins. We posit that ZFOURGE is detecting fainter sources in these redshift bins than have been previously observed in the literature. This is unlikely to be a result of incompleteness on our part, as all other redshift bins are in great agreement with the literature, showcasing that our methodology is sound. Best care has been taken to ensure the chosen bolometric flux limits align with the 24 μ m flux limit of 0.003mJy. From $1.7 \leq z < 2$, both Rodighiero *et al.* (2010) and Gruppioni *et al.* (2013) show a large drop in their faintest luminosity bins, consistent with an incomplete dataset. The same can be said in the redshift bin $3.0 \leq z < 4.2$; Gruppioni *et al.* (2013) sees a drop of $\approx 0.5 \log(\phi_*)$ or more in each luminosity bin of the LF when compared to their previous redshift bin and is very likely to be solely an incompleteness issue given it is their final redshift bin. The fact that both see a drop from $1.7 \leq z < 2$ gives credence to incompleteness at this redshift. Curiously, this does not seem to be a problem for either Gruppioni *et al.* (2013) or Rodighiero *et al.* (2010) in the redshift bins immediately before and after, or any other redshift bin for that matter. Rodighiero *et al.* (2010) utilises multiwavelength Spitzer observations whereas Gruppioni *et al.* (2013) uses Herschel/PACS data to estimate the total IR LF. Given that this incompleteness exists across multiple surveys and instruments, it remains to be seen why a drop in completeness at the $1.7 \leq z < 2$ redshift bin exists at all when neighbouring redshift bins show no sign of incompleteness.

Similar can be said about our redshift bin $4.2 \leq z < 6.0$. We do not have any luminosity bins along the faint end slope of our LF, and so the LF as a whole is poorly constrained with our three luminosity bins. The luminosity function drops considerably by $0.52 \log(\phi_*)$ in the brightest luminosity bin, suggesting this is due to incompleteness.

In figure 3 we show the combined evolution of the ZFOURGE bolometric IR (8-1000 μ m) LF. The LF is filled between the uncertainty calculated using equation 5. From this plot it is easier to see the evolution of the LF across luminosity and redshift. There is a clear downwards luminosity evolution trend with redshift seen. As redshift increases, the luminosity function indeed decreases. There are too few luminosity bins in the redshift bin $4.2 \leq z < 6.0$ to accurately constrain the LF and where there is also a corresponding drop in number density. As shown in Gruppioni et al. (2013) and Rodighiero et al. (2010), there is also a significant drop in two of their redshift bins. This suggests our $4.2 \leq z < 6.0$ redshift bin is significantly impacted by incompleteness, and as such, should be taken as a lower limit.

5.2. Parameter Evolution

Here we discuss the parameter evolution of the Schechter and Saunders luminosity function fits in figure 2. We fix the faint and bright end slopes, α and σ respectively, across all redshift bins. The Schechter α is fixed to 1.2, and the Saunders α is fixed to 1.3. In the first two bins, $0.0 \leq z < 0.3$ and $0.3 \leq z < 0.45$, σ is fixed to 0.9, and in all other redshift bins is fixed to 0.6.

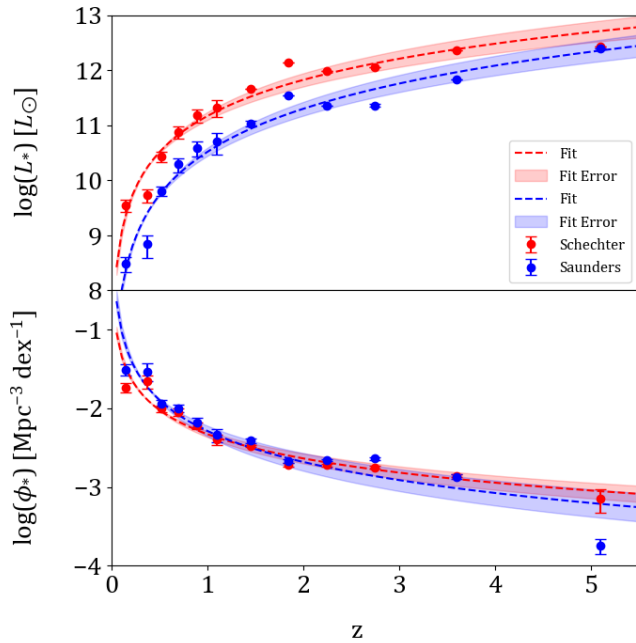


Figure 4. Best fit parameter evolution to the LF as a function of z : $y = a \log_{10}(z) + c$ for both Schechter (1976) and Saunders et al. (1990) fits with one standard deviation fit error. Top: L_* evolution - Schechter $\log_{10}(L_*) = 0.94^{0.07}_{0.07} \times \log_{10}(z) + 11.16^{0.07}_{0.07}$ and Saunders $\log_{10}(L_*) = 1.13^{0.07}_{0.07} \times \log_{10}(z) + 10.51^{0.07}_{0.07}$. Bottom: ϕ_* evolution - Schechter $\log_{10}(\phi_*) = -0.44^{0.04}_{0.04} \times \log_{10}(z) - 2.32^{0.04}_{0.04}$ and Saunders $\log_{10}(\phi_*) = -0.56^{0.07}_{0.07} \times \log_{10}(z) - 2.28^{0.07}_{0.07}$.

The evolution of ϕ_* and L_* are represented in figure 4 across redshift. These values were calculated using SciPy curve_fit (Virtanen et al. 2020) as the best fitting results of the Schechter (equation 6) and Saunders' (equation 7) functions. 1σ parameter uncertainties are calculated using `perr = np.sqrt(np.diag(pcov))` which relates the covariance of the best fit parameters.

We fit a simple log function $p = a \log_{10}(z) + c$ to each parameter to trace its evolution with redshift. Schechter L_* evolves

Table 4. Parameter evolution values as a function of redshift

	$\log(L_*)$	$\log(\phi_*)$	$\log(L_*)$	$\log(\phi_*)$
	Schechter	Schechter	Saunders	Saunders
0.150	9.54 ± 0.13	-1.74 ± 0.06	8.49 ± 0.15	-1.51 ± 0.07
0.375	9.72 ± 0.14	-1.66 ± 0.09	8.84 ± 0.25	-1.53 ± 0.13
0.525	10.43 ± 0.10	-2.00 ± 0.04	9.81 ± 0.10	-1.94 ± 0.05
0.700	10.88 ± 0.12	-2.05 ± 0.05	10.29 ± 0.14	-2.00 ± 0.05
0.900	11.18 ± 0.13	-2.22 ± 0.05	10.59 ± 0.16	-2.18 ± 0.06
1.100	11.32 ± 0.18	-2.40 ± 0.07	10.70 ± 0.24	-2.34 ± 0.09
1.450	11.65 ± 0.00	-2.48 ± 0.01	11.03 ± 0.06	-2.41 ± 0.03
1.850	12.14 ± 0.00	-2.72 ± 0.03	11.53 ± 0.00	-2.67 ± 0.02
2.250	11.98 ± 0.00	-2.72 ± 0.02	11.35 ± 0.00	-2.66 ± 0.01
2.750	12.05 ± 0.00	-2.75 ± 0.01	11.36 ± 0.03	-2.64 ± 0.02
3.600	12.37 ± 0.00	-2.86 ± 0.02	11.84 ± 0.00	-2.87 ± 0.03
5.100	12.44 ± 0.00	-3.15 ± 0.18	12.39 ± 0.00	-3.74 ± 0.11

as $\log_{10}(L_*) = 0.94^{0.07}_{0.07} \times \log_{10}(z) + 11.16^{0.07}_{0.07}$ and Saunders $\log_{10}(L_*) = 1.13^{0.07}_{0.07} \times \log_{10}(z) + 10.51^{0.07}_{0.07}$. Schechter ϕ_* evolution $\log_{10}(\phi_*) = -0.44^{0.04}_{0.04} \times \log_{10}(z) - 2.32^{0.04}_{0.04}$ and Saunders $\log_{10}(\phi_*) = -0.56^{0.07}_{0.07} \times \log_{10}(z) - 2.28^{0.07}_{0.07}$. Again, this fitting was performed with SciPy curve_fit as well as the 1σ uncertainty is calculated the same as before. The best fitting simple log functions are shown in figure 4 with 1σ parameter error outlined.

Importantly, the Saunders L_* fits follow a much steeper gradient evolution with redshift than the Schechter counterpart which is consistently far above the Saunders curve until the final redshift bin. As discussed in section 5.1, this redshift bin suffers from incompleteness. However, it is not clear that either the Schechter or Saunders L_* should be taken as a lower limit because 1σ parameter errors are 30 orders of magnitude smaller than both L_* 's from redshift bin $1.2 \leq z < 1.7$ and above. When compared to Gruppioni et al. (2013), a similar trend in L_* evolution with redshift is seen. In opposition to L_* , the ϕ_* evolution does not differ significantly between the Schechter or Saunders fits. Accompanying this result are the very low 1σ errors which are only pronounced at the smallest and highest redshift bins. Compared to Gruppioni et al. (2013), we find a different evolution of parameters below $z \approx 1$. Whilst our results indicate a shallow evolution in the first two redshift bins, our data follows a greater evolution and is better fit by a simple log function. Again, our final redshift bin suffers from incompleteness and so we consequently find a sharp decrease in ϕ_* , but this should be taken as a lower limit.

Our results indicate that the composition and evolution of the universe was relatively static above redshift $z \approx 3$ when the universe was approximately 2 Gyrs old. Since then, the characteristic density, ϕ_* , has increased from ≈ 0.00277 galaxies $\text{Mpc}^{-3} \text{dex}^{-1}$ at $z = 3$ to 0.0153 galaxies $\text{Mpc}^{-3} \text{dex}^{-1}$ at $z = 0.15$ when the universe was 11.58 Gyrs old. This represents a 5.52x increase in the number density of galaxies between these two times. The characteristic luminosity, L_* , similarly shows little evolution above $z = 3$ and evolves rapidly at lower redshifts.

5.3. Bolometric IR Luminosity Density

In this section, we calculate and analyse the total bolometric IR (8-1000 μ m) luminosity density, ρ_{IR} . At each redshift bin, ρ_{IR} is calculated by integrating under the bolometric IR LF. We utilise

`scipy.integrate.quad` (Virtanen et al. 2020) to perform the integration from 10^8 to $10^{14} L_{\odot}$. We calculate 1σ uncertainties as previously described by re-performing the integration using the relative 1σ upper and lower parameter errors.

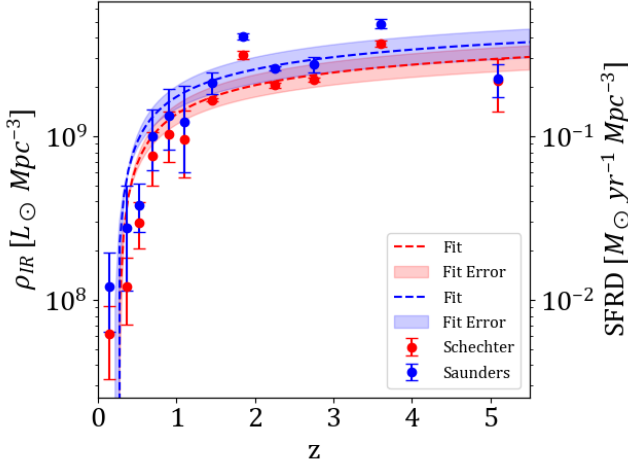


Figure 5. Evolution of the bolometric IR luminosity density calculated by integrating under the best fitting star-forming Schechter (1976) and Saunders et al. (1990) functions. Again we fit a simple function $y = a \log_{10}(z) + c$ and show one standard deviation fit errors. The best fitting parameters of the simple log function are $\rho_{IR} = 9.93^{1.89}_{1.89} \times 10^8 \log_{10}(z) + 1.36^{0.18}_{0.18} \times 10^9$ for Schechter, and $\rho_{IR} = 1.18^{0.27}_{0.27} \times 10^9 + 1.74^{0.27}_{0.27} \times 10^9$ for Saunders. The right side y-axis is obtained from Kennicutt (1998) by dividing ρ_{IR} by $1.7 \times 10^{10} L_{\odot}$.

Table 5. Bolometric IR (8-1000 μ m) density as a function of redshift.

z	$\rho_{IR} (L_{\odot} \text{ Mpc}^{-3})/10^8$	$\rho_{IR} (L_{\odot} \text{ Mpc}^{-3})/10^8$
	Schechter Fit	Saunders' Fit
0.150	$0.62^{0.29}_{0.29}$	$1.22^{0.73}_{0.57}$
0.375	$1.20^{0.62}_{0.50}$	$2.76^{2.25}_{1.62}$
0.525	$2.95^{1.02}_{0.89}$	$3.78^{1.35}_{1.17}$
0.700	$7.62^{3.00}_{2.58}$	$10.06^{4.57}_{3.85}$
0.900	$10.29^{3.82}_{3.32}$	$13.47^{6.14}_{5.16}$
1.100	$9.61^{4.87}_{4.02}$	$12.30^{8.01}_{6.26}$
1.450	$16.75^{0.41}_{0.41}$	$21.37^{3.30}_{3.09}$
1.850	$31.50^{1.73}_{1.73}$	$41.11^{1.81}_{1.81}$
2.250	$20.56^{0.80}_{0.80}$	$26.19^{0.83}_{0.83}$
2.750	$22.20^{0.74}_{0.74}$	$27.46^{3.00}_{2.86}$
3.600	$36.80^{1.47}_{1.47}$	$48.83^{3.04}_{3.04}$
5.100	$21.92^{7.67}_{7.67}$	$22.47^{5.16}_{5.16}$

Note: Redshift bin values are centred. Refer to tables 2 and ?? for ranges.

Figure 5 shows the evolution of the bolometric IR luminosity density as a function of redshift. We perform the calculation of ρ_{IR} for both the Schechter (equation 6) and Saunders (equation 7) functions using equations 9 and 10 with our results displayed in table 5. We use the star-forming luminosity function as our integration curve. The star-forming LF is not shown in figure 2 as it is very similar to the total IR LF, thus our SF IR density results are not expected to be very different from the total IR density, however, that would include contamination from non-star-forming galaxies. Figure 5 also displays a secondary right-hand-side axis which

is a scaling conversion factor to star-formation-rate provided by Kennicutt (1998) calculated by dividing ρ_{IR} by $1.7 \times 10^{10} L_{\odot}$.

$$\rho_{IR} = \int_{10^8}^{10^{14}} \varphi(L) = \varphi^* \left(\frac{L}{L^*} \right)^{1-\alpha} \exp \left(-\frac{L}{L^*} \right) \quad (9)$$

$$\rho_{IR} = \int_{10^8}^{10^{14}} \varphi^* \left(\frac{L}{L^*} \right)^{1-\alpha} \exp \left[-\frac{1}{2\sigma^2} \log_{10}^2 \left(1 + \frac{L}{L^*} \right) \right] \quad (10)$$

Our results in figure 5 show rapid evolution from $0 < z < 1$, after which evolution drastically slows down from $z > 1$ onwards. Our highest redshift bin suffers from incompleteness, so the ρ_{IR} is a lower limit at this redshift. Importantly, we do not find a turnover in the IR luminosity density as ρ_{IR} grows with redshift. This is a very different result than is often published in the literature (Gruppioni et al. 2013) [more sources here! reasons why their turns over](#) although this is not a new result (Rodighiero et al. 2010) [more sources here! reasons why their doesn't turn over](#)

6. Conclusion

Acknowledgements

Thank you to the anonymous referee that provided feedback on the paper.

Data Availability

Python notebooks and scripts that analysed the data are available on GitHub at <https://github.com/daniel-lyon/MPhil-Code>

References

- Assef, R. J., Kochanek, C. S., Ashby, M. L. N., Brodwin, M., Brown, M. J. I., Cool, R., Forman, W., Gonzalez, A. H., Hickox, R. C., Jannuzi, B. T., Jones, C., Le Floc'h, E., Moustakas, J., Murray, S. S., & Stern, D. 2011, The Mid-IR- and X-ray-Selected QSO Luminosity Function. *The Astrophysical Journal*, 728, 56. ADS Bibcode: 2011ApJ...728...56A.
- Astropy Collaboration, Price-Whelan, A. M., Lim, P. L., Earl, N., Starkman, N., Bradley, L., Shupe, D. L., Patil, A. A., Corrales, L., Brasseur, C. E., Nöthe, M., Donath, A., Tollerud, E., Morris, B. M., Ginsburg, A., Vaher, E., Weaver, B. A., Tocknell, J., Jamieson, W., van Kerkwijk, M. H., Robitaille, T. P., Merry, B., Bachetti, M., Günther, H. M., Aldcroft, T. L., Alvarado-Montes, J. A., Archibald, A. M., Bódi, A., Bapat, S., Barentsen, G., Bazán, J., Biswas, M., Boquien, M., Burke, D. J., Cara, D., Cara, M., Conroy, K. E., Conseil, S., Craig, M. W., Cross, R. M., Cruz, K. L., D'Eugenio, F., Dencheva, N., Devillepoix, H. A. R., Dietrich, J. P., Eigenbrot, A. D., Erben, T., Ferreira, L., Foreman-Mackey, D., Fox, R., Freij, N., Garg, S., Geda, R., Glattly, L., Gondhalekar, Y., Gordon, K. D., Grant, D., Greenfield, P., Groener, A. M., Guest, S., Gurovich, S., Handberg, R., Hart, A., Hatfield-Dodds, Z., Homeier, D., Hosseinzadeh, G., Jenness, T., Jones, C. K., Joseph, P., Kalmbach, J. B., Karamehmetoglu, E., Kałuszyński, M., Kelley, M. S. P., Kern, N., Kerzendorf, W. E., Koch, E. W., Kulumani, S., Lee, A., Ly, C., Ma, Z., MacBride, C., Maljaars, J. M., Muna, D., Murphy, N. A., Norman, H., O'Steen, R., Oman, K. A., Pacifici, C., Pascual, S., Pascual-Granado, J., Patil, R. R., Perren, G. I., Pickering, T. E., Rastogi, T., Roulston, B. R., Ryan, D. F., Rykoff, E. S., Sabater, J., Sakurikar, P., Salgado, J., Sanghi, A., Saunders, N., Savchenko, V., Schwardt, L., Seifert-Eckert, M., Shih, A. Y., Jain, A. S., Shukla, G., Sick, J., Simpson, C., Singanamalla, S., Singer, L. P., Singhal, J., Sinha, M., Sipőcz, B. M., Spitler, L. R., Stansby, D., Streicher, O., Šumak, J., Swinbank, J. D., Taranu, D. S., Tewary, N., Tremblay, G. R., de Val-Borro, M., Van Kooten, S. J., Vasović, Z., Verma, S., de Miranda Cardoso, J. V., Williams, P. K. G., Wilson, T. J., Winkel, B., Wood-Vasey, W. M., Xue, R., Yoachim, P., Zhang, C., Zonca, A., & Astropy Project Contributors 2022, The Astropy Project: Sustaining and Growing a Community-oriented Open-source Project and the Latest Major Release

- (v5.0) of the Core Package. *The Astrophysical Journal*, 935, 167. ADS Bibcode: 2022ApJ...935..167A.
- Biviano, A., Fadda, D., Durret, F., Edwards, L. O. V., & Marleau, F. 2011, Spitzer observations of Abell 1763. III. The infrared luminosity function in different supercluster environments. *Astronomy and Astrophysics*, 532, A77.
- Brown, A., Nayyeri, H., Cooray, A., Ma, J., Hickox, R. C., & Azadi, M. 2019, Infrared Contributions of X-Ray Selected Active Galactic Nuclei in Dusty Star-forming Galaxies. *The Astrophysical Journal*, 871, 87. ADS Bibcode: 2019ApJ...871...87B.
- Cowley, M. J., Spitler, L. R., Tran, K.-V. H., Rees, G. A., Labbé, I., Allen, R. J., Brammer, G. B., Glazebrook, K., Hopkins, A. M., Juneau, S., Kacprzak, G. G., Mullaney, J. R., Nanayakkara, T., Papovich, C., Quadri, R. F., Straatman, C. M. S., Tomczak, A. R., & van Dokkum, P. G. 2016, ZFOURGE catalogue of AGN candidates: an enhancement of 160-m-derived star formation rates in active galaxies to $z = 3.2$. *Monthly Notices of the Royal Astronomical Society*, 457, 629–641. ADS Bibcode: 2016MNRAS.457..629C.
- Dai, X., Assef, R. J., Kochanek, C. S., Brodwin, M., Brown, M. J. I., Caldwell, N., Cool, R. J., Dey, A., Eisenhardt, P., Eisenstein, D., Gonzalez, A. H., Jannuzi, B. T., Jones, C., Murray, S. S., & Stern, D. 2009, Mid-Infrared Galaxy Luminosity Functions from the AGN and Galaxy Evolution Survey. *The Astrophysical Journal*, 697, 506–521. ADS Bibcode: 2009ApJ...697..506D.
- Fu, H., Yan, L., Scoville, N. Z., Capak, P., Aussel, H., Le Floc'h, E., Ilbert, O., Salvato, M., Kartaltepe, J. S., Frayer, D. T., Sanders, D. B., Sheth, K., & Taniguchi, Y. 2010, Decomposing Star Formation and Active Galactic Nucleus with Spitzer Mid-infrared Spectra: Luminosity Functions and Co-evolution. *The Astrophysical Journal*, 722, 653–667. ADS Bibcode: 2010ApJ...722..653F.
- Giacconi, R., Zirm, A., Wang, J., Rosati, P., Nonino, M., Tozzi, P., Gilli, R., Mainieri, V., Hasinger, G., Kewley, L., Bergeron, J., Borgani, S., Gilmozzi, R., Grogin, N., Koekemoer, A., Schreier, E., Zheng, W., & Norman, C. 2002, Chandra Deep Field South: The 1 Ms Catalog. *The Astrophysical Journal Supplement Series*, 139, 369–410. ADS Bibcode: 2002ApJS...139..369G.
- Grazian, A., Fontana, A., Santini, P., Dunlop, J. S., Ferguson, H. C., Castellano, M., Amorin, R., Ashby, M. L. N., Barro, G., Behroozi, P., Boutsia, K., Caputi, K. I., Chary, R. R., Dekel, A., Dickinson, M. E., Faber, S. M., Fazio, G. G., Finkelstein, S. L., Galametz, A., Giallongo, E., Giavalisco, M., Grogin, N. A., Guo, Y., Kocevski, D., Koekemoer, A. M., Koo, D. C., Lee, K.-S., Lu, Y., Merlin, E., Mobasher, B., Nonino, M., Papovich, C., Paris, D., Pentericci, L., Reddy, N., Renzini, A., Salmon, B., Salvato, M., Sommariva, V., Song, M., & Vanzella, E. 2015, The galaxy stellar mass function at $3.5 < z < 7.5$ in the CANDELS/UDS, GOODS-South, and HUDF fields. *Astronomy and Astrophysics*, 575, A96.
- Gruppioni, C., Pozzi, F., Rodighiero, G., Delvecchio, I., Berta, S., Pozzetti, L., Zamorani, G., Andreani, P., Cimatti, A., Ilbert, O., Le Floc'h, E., Lutz, D., Magnelli, B., Marchetti, L., Monaco, P., Nordon, R., Oliver, S., Popesso, P., Riguccini, L., Roseboom, I., Rosario, D. J., Sargent, M., Vaccari, M., Altieri, B., Aussel, H., Bongiovanni, A., Cepa, J., Daddi, E., Domínguez-Sánchez, H., Elbaz, D., Förster Schreiber, N., Genzel, R., Iribarrem, A., Magliocchetti, M., Maiolino, R., Poglitsch, A., Pérez García, A., Sanchez-Portal, M., Sturm, E., Tacconi, L., Valtchanov, I., Amblard, A., Arumugam, V., Bethermin, M., Bock, J., Boselli, A., Buat, V., Burgarella, D., Castro-Rodríguez, N., Cava, A., Chianal, P., Clements, D. L., Conley, A., Cooray, A., Dowell, C. D., Dwek, E., Eales, S., Franceschini, A., Glenn, J., Griffin, M., Hatziminaoglou, E., Ibar, E., Isaak, K., Ivison, R. J., Lagache, G., Levenson, L., Lu, N., Madden, S., Maffei, B., Mainetti, G., Nguyen, H. T., O'Halloran, B., Page, M. J., Panuzzo, P., Papageorgiou, A., Pearson, C. P., Pérez-Fournon, I., Pohlen, M., Rigopoulou, D., Rowan-Robinson, M., Schulz, B., Scott, D., Seymour, N., Shupe, D. L., Smith, A. J., Stevens, J. A., Symeonidis, M., Trichas, M., Tugwell, K. E., Vigroux, L., Wang, L., Wright, G., Xu, C. K., Zemcov, M., Bardelli, S., Carollo, M., Contini, T., Le Fèvre, O., Lilly, S., Mainieri, V., Renzini, A., Scodreggio, M., & Zucca, E. 2013, The Herschel PEP/HerMES luminosity function - I. Probing the evolution of PACS selected Galaxies to $z = 4$. *Monthly Notices of the Royal Astronomical Society*, 432, 23–52. ADS Bibcode: 2013MNRAS.432...23G.
- Gruppioni, C., Pozzi, F., Zamorani, G., & Vignali, C. 2011, Modelling galaxy and AGN evolution in the infrared: black hole accretion versus star formation activity. *Monthly Notices of the Royal Astronomical Society*, 416, 70–86. ADS Bibcode: 2011MNRAS.416...70G.
- Han, Y., Dai, B., Wang, B., Zhang, F., & Han, Z. 2012, Evolution of the luminosity function and obscuration of active galactic nuclei: comparison between X-ray and infrared. *Monthly Notices of the Royal Astronomical Society*, 423, 464–477. ADS Bibcode: 2012MNRAS.423..464H.
- Katsianis, A., Blanc, G., Lagos, C. P., Tejos, N., Bower, R. G., Alavi, A., Gonzalez, V., Theuns, T., Schaller, M., & Lopez, S. 2017, The evolution of the star formation rate function in the EAGLE simulations: a comparison with UV, IR and H observations from $z = 8$ to $z = 0$. *Monthly Notices of the Royal Astronomical Society*, 472, 919–939. ADS Bibcode: 2017MNRAS.472..919K.
- Kennicutt, Jr., R. C. 1998, The Global Schmidt Law in Star-forming Galaxies. *The Astrophysical Journal*, 498, 541–552. Publisher: IOP ADS Bibcode: 1998ApJ...498..541K.
- Lawrence, A., Warren, S. J., Almaini, O., Edge, A. C., Hambly, N. C., Jameson, R. F., Lucas, P., Casali, M., Adamson, A., Dye, S., Emerson, J. P., Foucaud, S., Hewett, P., Hirst, P., Hodgkin, S. T., Irwin, M. J., Lodieu, N., McMahon, R. G., Simpson, C., Smail, I., Mortlock, D., & Folger, M. 2007, The UKIRT Infrared Deep Sky Survey (UKIDSS). *Monthly Notices of the Royal Astronomical Society*, 379, 1599–1617. ADS Bibcode: 2007MNRAS.379.1599L.
- Malmquist, K. G. 1922, On some relations in stellar statistics. *Meddelanden fran Lunds Astronomiska Observatorium Serie I*, 100, 1–52. ADS Bibcode: 1922MeLuF.100....1M.
- O'Connor, J. A., Rosenberg, J. L., Satyapal, S., & Secrest, N. J. 2016, The luminosity and stellar mass functions of red W1-W2 galaxies. *Monthly Notices of the Royal Astronomical Society*, 463, 811–819. ADS Bibcode: 2016MNRAS.463..811O.
- Persson, S. E., Murphy, D. C., Smee, S., Birk, C., Monson, A. J., Uomoto, A., Koch, E., Shectman, S., Barkhouser, R., Orndorff, J., Hammond, R., Harding, A., Scharfstein, G., Kelson, D., Marshall, J., & McCarthy, P. J. 2013, FourStar: The Near-Infrared Imager for the 6.5 m Baade Telescope at Las Campanas Observatory. *Publications of the Astronomical Society of the Pacific*, 125(928), 654. Publisher: University of Chicago Press.
- Rodighiero, G., Vaccari, M., Franceschini, A., Tresse, L., Le Fèvre, O., Le Brun, V., Mancini, C., Matute, I., Cimatti, A., Marchetti, L., Ilbert, O., Arnouts, S., Bolzonella, M., Zucca, E., Bardelli, S., Lonsdale, C. J., Shupe, D., Surace, J., Rowan-Robinson, M., Garilli, B., Zamorani, G., Pozzetti, L., Bondi, M., de la Torre, S., Vergani, D., Santini, P., Grazian, A., & Fontana, A. 2010, Mid- and far-infrared luminosity functions and galaxy evolution from multiwavelength Spitzer observations up to $z \sim 2.5$. *Astronomy and Astrophysics*, 515, A8. ADS Bibcode: 2010A&A...515A...8R.
- Saunders, W., Rowan-Robinson, M., Lawrence, A., Efstathiou, G., Kaiser, N., Ellis, R. S., & Frenk, C. S. 1990, The 60- μ m and far-infrared luminosity functions of IRAS galaxies. *Monthly Notices of the Royal Astronomical Society*, 242, 318–337. ADS Bibcode: 1990MNRAS.242..318S.
- Schechter, P. 1976, An analytic expression for the luminosity function for galaxies. *The Astrophysical Journal*, 203, 297–306. ADS Bibcode: 1976ApJ...203..297S.
- Schmidt, M. 1968, Space Distribution and Luminosity Functions of Quasi-Stellar Radio Sources. *The Astrophysical Journal*, 151, 393. ADS Bibcode: 1968ApJ...151..393S.
- Scoville, N., Aussel, H., Brusa, M., Capak, P., Carollo, C. M., Elvis, M., Giavalisco, M., Guzzo, L., Hasinger, G., Impey, C., Kneib, J. P., LeFevre, O., Lilly, S. J., Mobasher, B., Renzini, A., Rich, R. M., Sanders, D. B., Schinnerer, E., Schminovich, D., Shopbell, P., Taniguchi, Y., & Tyson, N. D. 2007, The Cosmic Evolution Survey (COSMOS): Overview. *The Astrophysical Journal Supplement Series*, 172, 1–8. ADS Bibcode: 2007ApJS...172....1S.
- Spitler, L. R., Labbé, I., Glazebrook, K., Persson, S. E., Monson, A., Papovich, C., Tran, K.-V. H., Poole, G. B., Quadri, R., van Dokkum, P., Kelson, D. D., Kacprzak, G. G., McCarthy, P. J., Murphy, D., Straatman, C. M. S., & Tilvi, V. 2012, First Results from Z-FOURGE: Discovery of a Candidate Cluster at $z = 2.2$ in COSMOS. *The Astrophysical Journal*, 748, L21. Publisher: IOP ADS Bibcode: 2012ApJ...748L...21S.

- Straatman, C. M. S., Spitler, L. R., Quadri, R. F., Labbé, I., Glazebrook, K., Persson, S. E., Papovich, C., Tran, K.-V. H., Brammer, G. B., Cowley, M., Tomczak, A., Nanayakkara, T., Alcorn, L., Allen, R., Broussard, A., Dokkum, P. v., Forrest, B., Houdt, J. v., Kacprzak, G. G., Kawinwanichakij, L., Kelson, D. D., Lee, J., McCarthy, P. J., Mehrrens, N., Monson, A., Murphy, D., Rees, G., Tilvi, V., & Whitaker, K. E. 2016, THE FOURSTAR GALAXY EVOLUTION SURVEY (ZFOURGE): ULTRAVIOLET TO FAR-INFRARED CATALOGS, MEDIUM-BANDWIDTH PHOTOMETRIC REDSHIFTS WITH IMPROVED ACCURACY, SLAR MASSES, AND CONFIRMATION OF QUIESCENT GALAXIES TO $z \sim 3.5$. *The Astrophysical Journal*, 830(1), 51. Publisher: The American Astronomical Society.
- Symeonidis, M. & Page, M. J. 2021, AGN and star formation across cosmic time. *Monthly Notices of the Royal Astronomical Society*, 503, 3992–4007. ADS Bibcode: 2021MNRAS.503.3992S.
- Virtanen, P., Gommers, R., Oliphant, T. E., Haberland, M., Reddy, T., Cournapeau, D., Burovski, E., Peterson, P., Weckesser, W., Bright, J., van der Walt, S. J., Brett, M., Wilson, J., Millman, K. J., Mayorov, N., Nelson, A. R. J., Jones, E., Kern, R., Larson, E., Carey, C. J., Polat, , Feng, Y., Moore, E. W., VanderPlas, J., Laxalde, D., Perktold, J., Cimrman, R., Henriksen, I., Quintero, E. A., Harris, C. R., Archibald, A. M., Ribeiro, A. H., Pedregosa, F., van Mulbregt, P., SciPy 1.0 Contributors, Vijaykumar, A., Bardelli, A. P., Rothberg, A., Hilboll, A., Kloeckner, A., Scopatz, A., Lee, A., Rokem, A., Woods, C. N., Fulton, C., Masson, C., Häggström, C., Fitzgerald, C., Nicholson, D. A., Hagen, D. R., Pasechnik, D. V., Olivetti, E., Martin, E., Wieser, E., Silva, F., Lenders, F., Wilhelm, F., Young, G., Price, G. A., Ingold, G.-L., Allen, G. E., Lee, G. R., Audren, H., Probst, I., Dietrich, J. P., Silterra, J., Webber, J. T., Slavič, J., Nothman, J., Buchner, J., Kulick, J., Schönberger, J. L., de Miranda Cardoso, J. V., Reimer, J., Harrington, J., Rodríguez, J. L. C., Nunez-Iglesias, J., Kuczynski, J., Tritz, K., Thoma, M., Newville, M., Kümmerer, M., Bolingbroke, M., Tartre, M., Pak, M., Smith, N. J., Nowaczyk, N., Shebanov, N., Pavlyk, O., Brodtkorb, P. A., Lee, P., McGibbon, R. T., Feldbauer, R., Lewis, S., Tygier, S., Sievert, S., Vigna, S., Peterson, S., More, S., Pudlik, T., Oshima, T., Pingel, T. J., Robitaille, T. P., Spura, T., Jones, T. R., Cera, T., Leslie, T., Zito, T., Krauss, T., Upadhyay, U., Halchenko, Y. O., & Vázquez-Baeza, Y. 2020, SciPy 1.0: fundamental algorithms for scientific computing in Python. *Nature Methods*, 17(3), 261–272.
- Wu, Y., Shi, Y., Helou, G., Armus, L., Dale, D. A., Papovich, C., Rahman, N., Dasyra, K., & Stierwalt, S. 2011, The Mid-infrared Luminosity Function at $z \sim 0.3$ from 5MUSES: Understanding the Star Formation/Active Galactic Nucleus Balance from a Spectroscopic View. *The Astrophysical Journal*, 734(1), 40.
- Wuyts, S., Labbé, I., Förster Schreiber, N. M., Franx, M., Rudnick, G., Brammer, G. B., & van Dokkum, P. G. 2008, FIREWORKS U38-to-24 m Photometry of the GOODS Chandra Deep Field-South: Multiwavelength Catalog and Total Infrared Properties of Distant Ks-selected Galaxies. *The Astrophysical Journal*, 682, 985–1003. Publisher: IOP ADS Bibcode: 2008ApJ...682..985W.
- Wylezalek, D., Vernet, J., De Breuck, C., Stern, D., Brodwin, M., Galametz, A., Gonzalez, A. H., Jarvis, M., Hatch, N., Seymour, N., & Stanford, S. A. 2014, The Galaxy Cluster Mid-infrared Luminosity Function at $1.3 < z < 3.2$. *The Astrophysical Journal*, 786, 17. ADS Bibcode: 2014ApJ...786...17W.